The Competition Between Mechanical Stability and Charge Carrier Mobility in MA-based Hybrid Perovskites: Insight from DFT

Jung-Hoon Lee,*‡[a] Zeyu Deng,‡[a] Nicholas C. Bristowe,[b,c]
Paul D. Bristowe,*[a] and Anthony K. Cheetham*[a]

[a]*Department of Materials Science and Metallurgy, University of Cambridge, Cambridge CB3 0FS, UK*

[b]*School of Physical Sciences, University of Kent, Canterbury CT2 7NH, UK*

[c]*Department of Materials, Imperial College London, London SW7 2AZ, UK*

*E-mail: jhlee.david@gmail.com, pdb1000@cam.ac.uk, akc30@cam.ac.uk.

‡These authors contributed equally.

†Electronic Supplementary Information (ESI) available. 10.1039/b000000x/

Abstract

Hybrid organic-inorganic perovskites and their inorganic analogues, such as $MAPbI_3$ (MA = methylammonium, CH_3NH_3) and $CsPbI_3$, are currently under intense investigation due to their high-power conversion efficiencies and low cost for solar cell applications. Herein, we investigate the effect of methylammonium and the inorganic A-cations on the elastic and related transport properties of halide perovskites using van der Waals (vdW) corrected density functional theory (DFT) calculations. For inorganic halide perovskites

we find that the bonding within the inorganic framework is mainly responsible for their elastic behavior. However, our DFT calculations show that when a MA cation is substituted into the structure the combined effects of stericity (conformation) and hydrogen-framework interactions improve the material's resistance to deformation. For example, the orientationally-averaged Young's modulus of orthorhombic $MAPbI_3$ increases by about 19 % compared to the equivalent inorganic series of structures. We also find that, within the carrier-acoustic phonon scattering regime, the electron and hole carrier mobilities of hybrid halide perovskites are lowered by the hydrogen-bonding-induced tilting of the inorganic octahedra. Taken together, these results can help guide the optimization of the mechanical and transport properties of perovskite-based solar cell materials.

1. Introduction

Over the last few years, hybrid organic-inorganic perovskite-based solar cells have received a great deal of attention due to their high electrical power conversion efficiencies (PCEs). These PCEs have reached 22.7 % in 2018[1] up from 3.8 % in 2009.[2] The high PCEs of hybrid perovskites have been attributed to their large absorption coefficients, long carrier diffusion lengths, high carrier mobilities, and suitable band gaps.[3–6] These fundamental properties are strongly related to key structural distortions within the perovskite unit cell (e.g., tilting of the inorganic octahedra). Previous experimental[7] and theoretical[8–10] studies have shown that the band gaps of halide perovskites can be tuned by adjusting the degree of octahedral tilting. In particular, the optical band gap increases as the degree of octahedral tilting increases. Furthermore, our own

previous work has predicted that octahedral tilting increases the effective electron mass, an important quantity affecting electrical conductivity.[10] In hybrid halide perovskites containing the methylammonium cation (MA, CH_3NH_3), this octahedral tilting is amplified by hydrogen-bonding interactions between the amine cation and the inorganic framework.[10–12] These results indicate that hydrogen-bonding can dramatically change the atomic structure within the unit cell, which in turn has a significant effect on the fundamental photovoltaic properties of these materials.

Recently, Motta et al.[13] showed that the band gap of cubic $MAPbI_3$ becomes indirect when the MA cation orients along the [011] direction. This indirect band gap is caused by Rashba splitting, a direct result of hydrogen-bonding-induced inversion symmetry breaking.[14,15] In addition, hydrogen-bonding plays a key role in the photostriction mechanism. According to a previous experimental study,[16] the photons induce charge transfer from the valence band maximum, which is composed of Pb 6*s*–I 5*p* hybridized orbitals, to the conduction band minimum, composed of Pb 6*p* orbitals. This transition weakens the hydrogen-bonding interactions between the three H ions bonded to N in the MA cation and three neighboring I ions due to an electron density reduction on the I sites, and then makes the Pb–I interatomic length longer. Interestingly, the MA cation itself can also affect the electrical transport properties of hybrid halide perovskites without any lattice distortion. In particular, Ma and Wang have proposed that the carrier mobility of the tetragonal $MAPbI_3$ phase is influenced by the randomly-oriented MA cation, causing a fluctuation of the electrostatic potential.[17] It is also worth noting that hydrogen-bonding and the structural distortion caused by the MA cation are closely related to the

material's elastic properties, although the details have yet to be investigated thoroughly. Previous studies[18–20] have shown that molecular cations dramatically enhance the elastic response of hybrid framework materials, particularly those with the perovskite architecture. Furthermore, this elastic enhancement can affect the electrical transport properties of the material within the acoustic-phonon scattering regime.[21–24] Hence, it is of fundamental importance to clearly elucidate the effect of the MA cation on both the elastic and transport properties of hybrid perovskites. Despite extensive previous studies,[21,22,31–40,23–30] our understanding of the role of the MA cation on these properties is still lacking.

In the present investigation, we use van der Waals (vdW) corrected DFT calculations to (i) identify how the MA cation influences the octahedral distortion of the structure and (ii) compute and understand the effect of this cation on the material's mechanical and transport properties, namely the elastic moduli and carrier mobilities. Here we adopt the orthorhombic structural model for all halide perovskites considered since the MA cations are ordered in the orthorhombic phase.[41] The systems studied are ABX_3 and $MABX_3$, where A = K, Rb, Cs and Fr, and B = Sn and Pb. The X-site halogens are Cl, Br and I. Choosing the orthorhombic model consistently across the series allows us to accurately predict the contribution of the MA cation to the fundamental properties of these perovskites. We acknowledge that some of these materials might not exist experimentally or do not normally adopt the orthorhombic perovskite structure, but the aim is to explore trends in behavior. Although the MA cations are disordered in the higher temperature tetragonal and cubic phases, our results are relevant to the these phases, too, because the MA-induced lattice distortion

can dynamically appear in them as well.[42,43] In summary, the main purpose of this contribution is to clarify the above-mentioned issues using vdW-corrected DFT calculations. We find that the combined effects of steric and hydrogen-bonding interactions of the MA cations enhance the elastic properties of the hybrid perovskites relative to their inorganic counterparts. Moreover, MA-induced octahedral tilting increases the effective carrier masses which results in a reduction in carrier mobility.

2. Methods

To quantitatively understand the effect of the MA organic cation, all the DFT calculations used the projector augmented-wave (PAW)[44,45] pseudopotentials as supplied in the Vienna Ab Initio Simulation Package (VASP).[46–49] The van der Waals functional (optB86b-vdW) was used in the relaxation process and calculation of the elastic moduli. This functional reproduces the experimental lattice parameters[41] of the orthorhombic(*o*-) $MAPbI_3$ structure better than other functionals like PBEsol, vdW-DF2, PBE+TS, and SCAN (see Table S1). The fractional coordinates of the atoms also compare well with experimental values. The electronic properties, including effective masses and deformation potentials, were calculated with the PBE functional along with spin-orbit coupling (SOC).[50] The following parameters were adopted: a 5×4×5 Monkhorst-Pack k-point mesh centered at Γ and a 1000 eV plane-wave kinetic energy cutoff, leading to a stress tensor converged to 0.1 kbar. The number of valence electrons treated explicitly were as follows: 14 for Pb ($5d^{10}6s^26p^2$), 14 for Sn ($4d^{10}5s^25p^2$), 7 for I ($5s^25p^5$), 7 for Br ($4s^24p^5$), 7 for Cl ($3s^23p^5$), 9 for K ($3s^23p^64s^1$), 9 for Rb ($4s^24p^65s^1$), 9 for Cs ($5s^25p^66s^1$), 9 for Fr ($6s^26p^67s^1$), 4

for C ($2s^2 2p^2$), 5 for N ($2s^2 2p^3$), and 1 for H ($1s^1$). The ions were relaxed until the forces on them were less than 0.01 eV $Å^{-1}$. The computed lattice parameters of all ground state structures are given in Table S3. In order to be self-consistent we determined the tolerance factor directly from our DFT electron density, defining the ionic radii by the volume of a sphere which contains 95% of the electron density, following previous DFT studies.[9,10] The ionic radii and calculated tolerance factors are shown in Table S2 and S3. All schematic representations of the crystal structures were generated using the VESTA program.[51]

The elastic moduli can be obtained from the generalized form of Hooke's law, which describes the relationship between stress σ and strain ε:

$$\sigma_i = C_{ij}\varepsilon_j \quad (1)$$

where C_{ij} is the single crystal stiffness tensor. Here the Voigt notation is adopted. C_{ij} is calculated using the following procedure: (i) fully relax both the unit cell volume and atomic positions and then (ii) apply strains to the optimized cell. When applying the strains to the unit cell, six different strain types are employed: ε_1, ε_2, ε_3, ε_4, ε_5, and ε_6 (see SI). For each strain, seven deformations are used: 0 %, ±0.5 %, ±1 % and ±1.5 %. Then, (iii) relax the atoms while fixing the deformed lattice parameters. By doing so, we can get stress tensors σ_{ij} for all applied strains ε_{ij}. Finally, (iv) C_{ij} are obtained from linear least-squares fitting using the stress-strain relationship. The computed C_{ij} values are given in Table S4. In order to calculate the polycrystalline moduli, we need the single crystal compliance tensor S_{ij}:

$$S_{ij} = C_{ij}^{-1} \quad (2)$$

The computed S_{ij} values are given in Table S5. After obtaining C_{ij} and S_{ij}, the polycrystalline (orientationally-averaged) elastic moduli, including the Young's modulus *E*, bulk modulus *B*, shear modulus *G*, and Poisson's ratio *v*, can be simply estimated as follows, where *V* denotes the Voigt upper bound and *R* the Reuss lower bound:[52]

$$B_V = \frac{1}{9}[(C_{11} + C_{22} + C_{33}) + 2(C_{12} + C_{13} + C_{23})] \quad (3)$$

$$B_R = \frac{1}{(S_{11}+S_{22}+S_{33})+2(S_{12}+S_{13}+S_{23})} \quad (4)$$

$$G_V = \frac{1}{15}[(C_{11} + C_{22} + C_{33}) - (C_{12} + C_{13} + C_{23}) + 3(C_{44} + C_{55} + C_{66})] \quad (5)$$

$$G_R = \frac{15}{4(S_{11}+S_{22}+S_{33})-4(S_{12}+S_{13}+S_{23})+3(S_{44}+S_{55}+S_{66})} \quad (6)$$

From the upper and lower bounds, the Voigt-Reuss-Hill (VRH) averages can be obtained for an isotropic material:

$$B = B_{VRH} = \frac{B_R+B_V}{2} \quad (7)$$

$$G = G_{VRH} = \frac{G_R+G_V}{2} \quad (8)$$

$$E = E_{VRH} = \frac{9B_{VRH}G_{VRH}}{3B_{VRH}+G_{VRH}} \quad (9)$$

$$\nu = \nu_{VRH} = \frac{3B_{VRH}-2G_{VRH}}{6B_{VRH}+2G_{VRH})} \quad (10)$$

Finally, the directional dependence of the Young's modulus ($E(\boldsymbol{u})$) in the *ab*, *bc* and *ca* planes of the orthorhombic structure was obtained using

$$E(\boldsymbol{u}) = \frac{1}{S'_{1111}(\boldsymbol{u})} = \frac{1}{u_{1i}u_{1j}u_{1k}u_{1l}S_{ijkl}} \quad (11)$$

where $\boldsymbol{u}$ is a unit vector and *S'* is the rotated elastic compliance tensor.

This index can be used to represent the hydrogen-bonding strength, and

for the case of hydrogen atoms attached to the nitrogen atom of the MA molecule, it can be evaluated as follows:[53]

$$\text{H-index} = \frac{f_{MAPbI_3}(N-H) - f_{MA}(N-H)}{f_{MA}(N-H)} \tag{12}$$

where $f_{\mathrm{MA}}(N-H)$ denotes the N–H stretching vibration frequency of a MA molecule in isolation (e.g. contained in a large empty supercell) and $f_{MAPbI_3}(N-H)$ refers to the corresponding frequency of a MA molecule experiencing hydrogen-bonding interactions with its neighboring I ions (N–H···I) in the PbI_3 framework of an orthorhombic (*o*-)$MAPbI_3$ unit cell. The equivalent equation could be written for the hydrogen atoms attached to the carbon atom of the MA molecule, but previous studies[11] on *o*-$MAPbI_3$ have indicated that hydrogen-bond interactions are larger on nitrogen. Thus, we can use equation (12) as an overall indicator of the hydrogen-bonding strength in a given hybrid halide perovskite by simply focusing on nitrogen and taking the mean of the three H-indices corresponding to the three hydrogens attached to this atom.

The charge carrier mobility μ_{ij} is calculated using the theory of deformation potentials[54] which considers carrier-phonon coupling in the acoustic regime as the dominant charge carrier scattering mechanism:

$$\mu_{ij} = \frac{(8\pi)^{1/2}\hbar^4 e C_{ij}}{3(m_{ij}^*)^{5/2}(k_B T)^{3/2} D_{ij}^2} \tag{13}$$

where e is the charge and C_{ij}, m_{ij}*, and D_{ij} are the stiffness tensor, the effective mass tensor, and the deformation potential tensor, respectively. m_{ij}* is

calculated from a numerical second order derivative of the band dispersion [$\partial^2 E(k)/\partial k^2$]. In order to obtain this, we use five eigenvalues near the valence (conduction) band maxima (minima) located at the Γ-point [0, 0, 0], from Γ to X = [0.5, 0, 0], Γ to Y = [0, 0.5, 0] and Γ to Z = [0, 0, 0.5] in the first Brillouin zone. The number of *k*-points between two *k*-points is forty. The effect of spin-orbit coupling is considered. Using a linear relationship between eigenvalue and strain, D_{ij} can be obtained. We apply the ε_1, ε_2, and ε_3 strains to the optimized orthorhombic unit cell and fix all internal coordinates. For each strain, five deformations are used: 0 %, ±0.5 % and ±1 %. By doing so, we can get D_{ij} values for each of the perovskites considered (see Table S6). All eigenvalues are aligned with the 1*s* core levels of the halogens (X = I, Br, Cl).

3. Results and Discussion

Figure 1(a) depicts the orthorhombic perovskite structure (space group *Pnma*) composed of BX_6 octahedra and A-site cations. It is characterized by the octahedral tilt pattern ($a^-b^+a^-$).[55] As shown in the figure, there exist two different types of X-site ion associated with the BX_6 octahedra: (i) an apical X-site ion along the *b*-axis in the *Pnma* setting (labeled X_A) and (ii) an equatorial X-site ion located on the BX_6 octahedral plane (labeled X_E). This results in two different bond angles between the B sites and the X sites: B-X_A-B and B-X_E-B. In order to capture the effect of octahedral tilting through these bond angles, we have computed a weighted average bond angle defined by $\theta_w = [4\theta(B - X_A - B) + 8\theta(B - X_E - B)]/12$. The weighting accounts for the relative multiplicity of X_A and X_E sites. Figure 1(b) shows θ_w as a function of the tolerance factor for all compositions. It is seen that octahedral tilting as defined

by θ_w increases as the tolerance factor becomes smaller (θ_w = 180° refers to an untilted structure). This means that steric effects dominate octahedral tilting in halide perovskites. More importantly, Figure 1(b) and Figure S1 demonstrate that hybrid halide perovskites have octahedra that are more tilted compared to inorganic halide perovskites with the same tolerance factor. This is because hydrogen-bonding amplifies octahedral tilting in hybrid halide perovskites.[10,11] Sn-based and Pb-based halide perovskites exhibit similar behavior. Thus, one can conclude that the hydrogen-bonding-induced octahedral tilting is a common feature of hybrid halide perovskites. This is consistent with our previous work.[10]

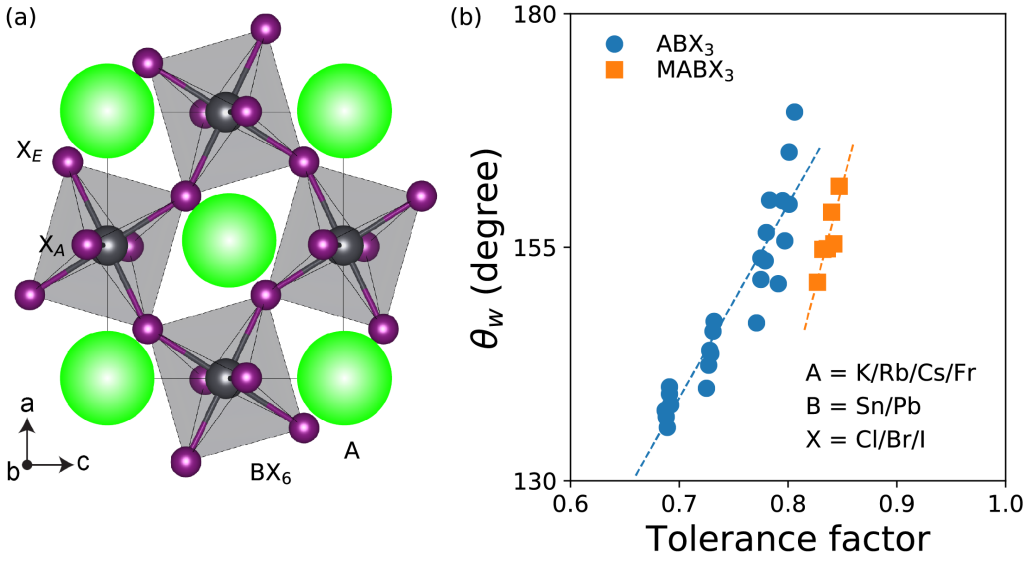

Figure 1 | Hydrogen-bonding-induced octahedral tilting. (a) The orthorhombic *Pnma* perovskite structure consisting of BX_6 octahedra (grey) and A site cations (green). (b) Computed weighted average bond angles (θ_w) between B-X_A-B and B-X_E-B as a function of the tolerance factor. Blue and orange symbols correspond to the *o*-ABX_3 inorganic and *o*-$MABX_3$ hybrid halide perovskites, respectively.

Figure S1 shows that the angular deviation from the trend line increases across the halogen series (I – Br – Cl) due to the increasing electronegativity of

the X-site halogen anion. The electronegativity increases in the sequence I–Br–Cl, and this increase enhances the hydrogen-bonding interaction and hence the tilting. The octahedra in the inorganic Pb phases are slightly more tilted than in the Sn phases, but the results for the MA phases indicate that the hydrogen bonding effect is nevertheless greater for Sn compared to Pb, as judged by the distances below the dotted lines for the MA systems in Figure S1. The electronegativity of Sn is less than that of Pb[56] and so the X-site halogen anion bonded to Sn tends to have more electron density compared to that bonded to Pb. Hence the Sn-based hybrid halide perovskites have slightly stronger hydrogen-bonds than the Pb-based hybrid halide perovskites. These trends agree well with our computed bond angle θ_w, H-index, and non-covalent interaction calculations (see Figures S1, S2, and S3). This hydrogen-bonding-induced lattice distortion and hydrogen-bonding itself may affect structural properties and electronic structure. Therefore, it is very important to quantitatively understand the effect of the MA cation on the elastic and transport properties of hybrid halide perovskites.

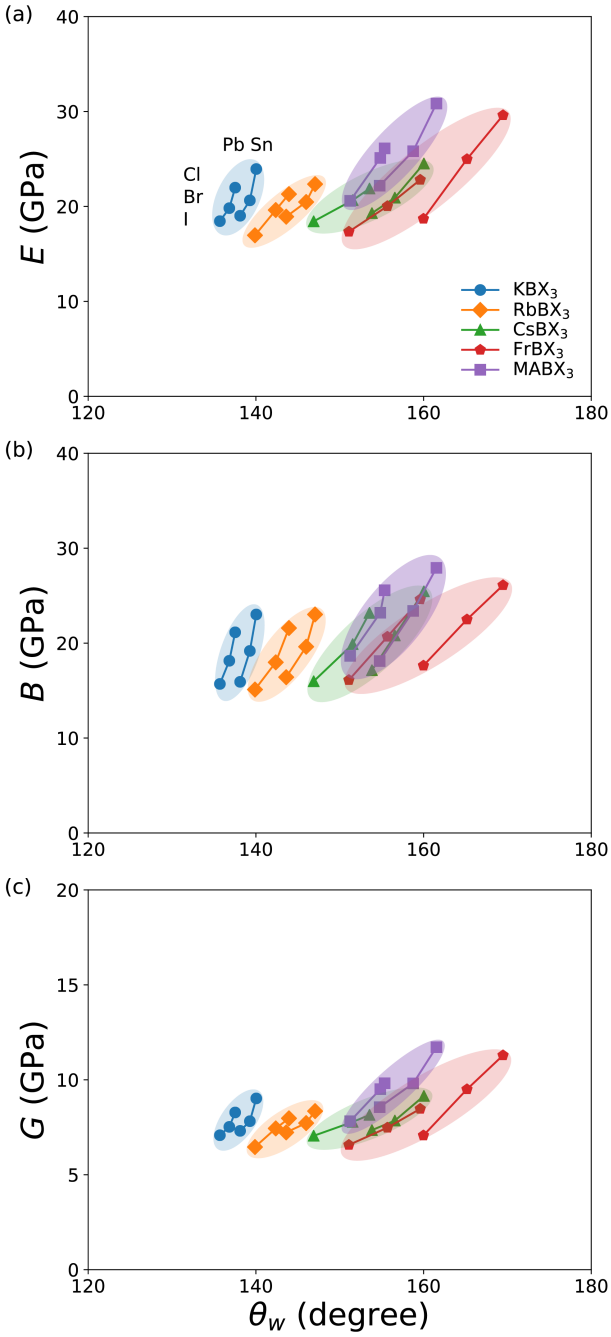

Figure 2 | Effect of chemical substitution on the isotropic polycrystalline elastic moduli of halide perovskites. (a) Young's modulus *E*, (b) bulk modulus *B*, and (c) shear modulus *G* as a function of θ_w for the *o*-ABX_3 inorganic and *o*-$MABX_3$ hybrid series. Different colors refer to different A-site cations.

Having demonstrated how the MA cation influences the lattice distortion of the perovskite structure, we now examine the elastic moduli of both the inorganic *o*-ABX_3 and hybrid *o*-$MABX_3$ series. By way of illustration, Figure S4

compares the directionally dependent Young's modulus *E* of *o*-$MAPbI_3$ and *o*-$CsPbI_3$. It is seen that both perovskites exhibit highly anisotropic moduli but that the shapes of the curves are very similar particularly in terms of the directions of the maxima and minima. Any differences are due to hydrogen bonding or steric effects as discussed below. However, the overall similarity of the curves shows that the PbI_3 inorganic framework is mainly responsible for the stiffness of *o*-$MAPbI_3$.

Based on this, we address the effect of chemical substitution on the elastic properties of the halide perovskites. Figure 2 shows the computed polycrystalline (orientationally-averaged) Young's modulus *E*, bulk modulus *B*, and shear modulus *G* as a function of θ_w. The numerical values are given in Table S3. In Figure 2, we can clearly see that the elastic moduli generally increase as the X anion is substituted in the sequence I – Br – Cl.[25] In addition, Sn-based halide perovskites have larger moduli than Pb-based halide perovskites. This is because the B-X bond strength increases as the ionic radii of the B- and X-site ions decreases. However, the A-site cations do not contribute as much to the elastic moduli as the B and X-site cations. Interestingly, for *o*-$FrSnBr_3$ and *o*-$FrSnCl_3$, all the polycrystalline moduli are larger than those of other Sn-based halide perovskites. This is because Fr ions fit well into the SnX_3 cages compared to other inorganic halide perovskites, making their structures more close-packed. The large tolerance factors of *o*-$FrSnBr_3$ and *o*-$FrSnCl_3$ (over 0.8) and their average bond angles θ_w (about 170^o) also support this. More interestingly, the polycrystalline moduli of the hybrid halide perovskites are generally larger than those of the inorganic halide perovskites, as seen in Figure 2, where purple squares corresponding to the

former are slightly above others in the series. This indicates that the MA cation enhances the elastic properties of hybrid halide perovskites, which we address in more detail in the next section.

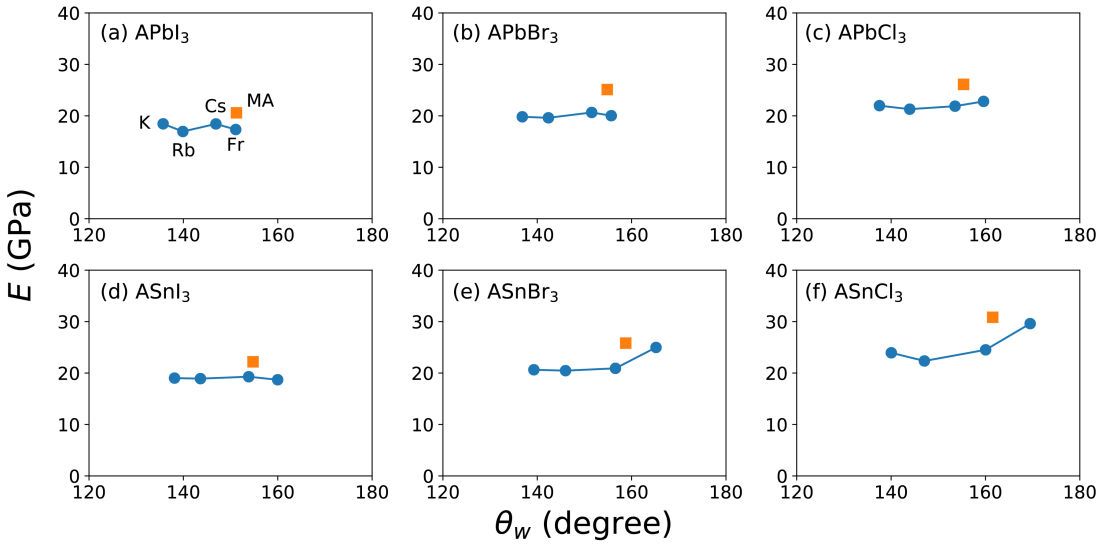

Figure 3 | Effect of the MA cation on Young's modulus *E*. The orientationally-averaged Young's modulus E versus θ_w for (a) *o*-$APbI_3$, (b) *o*-$APbBr_3$, (c) *o*-$APbCl_3$, (d) *o*-$ASnI_3$, (e) *o*-$ASnBr_3$, and (f) *o*-$ASnCl_3$. Blue and orange symbols correspond to the *o*-ABX_3 inorganic and *o*-$MABX_3$ hybrid perovskites respectively.

To understand quantitatively how the MA cation influences the elastic properties of hybrid halide perovskites, we consider, for each halide series, how the three main moduli *E, B* and *G* vary as a function of θ_w. Figure 3 illustrates the polycrystalline Young's modulus *E* where the orange symbols distinguish the hybrid perovskites from the inorganic perovskites shown in blue. The results for the bulk modulus *B* and shear modulus *G* are given in the SI (Figure S5 and S6). The values for the hybrid perovskites are similar to those computed previously[37] as are the trends in behavior, e.g. the elastic moduli of the hybrid bromides are greater than the hybrid iodides. Figure 3 shows that the Young's

moduli of the hybrid perovskites are always larger than those of inorganic perovskites, indicating their relative stiffness. The same effect is seen for the bulk and shear moduli showing that hybrid perovskites are also more resistant to hydrostatic pressure and shear deformation. Focusing on the Young's moduli, we see that for *o*-$MAPbI_3$, for example, *E* increases by about 19 % compared to the inorganic trend line at the same θ_w. In fact, this enhancement is caused by a combination of effects, one due the stericity (conformation) of the MA cation and the other due hydrogen-bonding interactions. Unlike other A-site inorganic cations, the shape of the MA cation is not spherical but approximately cylindrical.[10] In particular, there are six H atoms attached to the C-N bond and these H atoms, which point in different directions, have an important affect the perovskite's stiffness. Taking *o*-$MAPbI_3$ as an example, two of the H atoms forming the MA cation are oriented towards the *c*-axis of the perovskite while the other four are oriented towards the *b*-axis, as shown in Figure S7. Because of this, the stiffness components C_{22} and C_{33} of *o*-$MAPbI_3$ are larger than those of the inorganic iodide perovskites (see Table S4), and the same is true within the other halogen groups as well. Thus, the unique conformation of the MA cation makes a significant contribution to the elasticity of hybrid halide perovskites. Furthermore, of course, the H atoms forming the MA cations interact with neighboring halogens via hydrogen bonds. We suggest that this additional interaction also enhances the elastic properties although it is difficult to separate hydrogen-bonding effects from steric effects. Nevertheless, there is clear experimental evidence that the organic cation plays an important role. For instance, the measured Young's modulus of cubic $MAPbBr_3$ (15.6-21.4 GPa) is significantly larger than that of cubic $FAPbBr_3$ (9.7-12.3 GPa) and this

can be attributed to the higher symmetry of the FA ($CH(NH_2)_2$) cation and its weaker hydrogen-bonding interaction.[57]

Following the above discussion, we would expect an increase in the Young's modulus of a hybrid halide perovskite to also increase its charge carrier mobility. This is based on deformation potential theory,[54] which relates elastic properties and carrier-phonon interactions to mobility and is represented by Eq. (13) above. At the same time, however, hydrogen-bonding-induced octahedral tilting can reduce the carrier mobility since it increases the charge effective mass.[10] Therefore, it is important to understand how the MA cation affects the charge transport properties of hybrid halide perovskites. We address this in more detail in the following section.

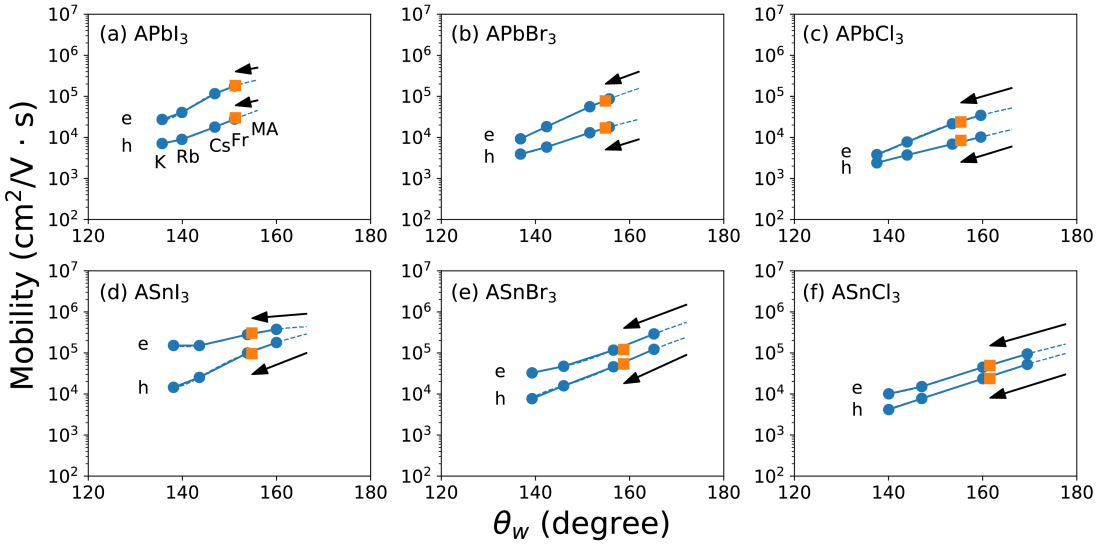

Figure 4 | Reduction of mobility due to MA-induced octahedral tilting. Average electron (e) and hole (h) mobilities along the three crystal axes versus θ_w for (a) *o*-$APbI_3$, (b) *o*-$APbBr_3$, (c) *o*-$APbCl_3$, (d) *o*-$ASnI_3$, (e) *o*-$ASnBr_3$, and (f) *o*-$ASnCl_3$. Blue and orange symbols correspond to the *o*-ABX_3 inorganic and *o*-$MABX_3$ hybrid halide perovskites, respectively. Arrows indicate the reduction in the e and h mobilities of *o*-$MABX_3$ with respect to what they would have been for hypothetical *o*-ABX_3 perovskites having the same size A-site cation. The lengths of the arrows correspond to the variations in the inorganic trend lines

shown in Fig. S1. The values are calculated at 100 K and shown in Table S8. The results obtained at 300 K are given in Table S9 and Figure S10.

We have calculated the charge carrier mobilities of all the halide perovskites considered in this study within the acoustic phonon scattering regime of deformation potential theory.[54] The aim is to predict trends in behavior with respect to chemical changes rather than reproduce experimental values. This is because other scattering mechanisms, such as optical phonons, defects, impurities or polarons, could be playing a role. In addition, of course, we have adopted the orthorhombic structure for all halide perovskites considered since the MA cations are ordered in this phase. However, we believe that carrier-acoustic phonon scattering is appropriate at low temperatures (~100K) where, for example, the *o*-$MAPbI_3$ structure is stable. At room temperature, there is evidence that scattering in tetragonal $MAPbI_3$ is dominated by carrier-optical phonon scattering.[36] Nevertheless the topic continues to be discussed both theoretically and experimentally.[29,31,36,37] For example, several studies[21–24,28] have highlighted the importance of carrier-acoustic phonon coupling even at room temperature where mobilities in tetragonal $MAPbI_3$ have been observed[21,58–60] to be proportional to $T^{-1.2}$ – $T^{-1.6}$.

In order to compute carrier mobilities (both electron and hole) using deformation potential theory, we need to determine the corresponding deformation potentials and effective carrier masses along each crystal axis. The results for the potentials and masses are given in Tables S6 and S7, respectively, and are comparable to values computed previously and experimental measurements.[23,24,28,31] These values can then be used in Eq. (13), together with the corresponding stiffness tensor components C_{ij}, to obtain

the electron and hole mobilities for all the halide perovskites considered (Table S8). Figure 4 shows the computed mobilities averaged along the three crystal axes as a function of θ_w for each halide series. It is clearly seen that the average carrier mobilities increase with increasing average bond angle, i.e. decreasing octahedral tilt (recall that θ_w = 180° refers to an untilted structure). This is consistent with measurements in other perovskite systems, e.g. doped-$LaCoO_3$, where the carrier mobility is found to increase as θ_w approaches 180°.[61] Figure 4 also shows that the electron mobility is always larger than the hole mobility for all halide perovskites. Our calculated mobilities are comparable with previous computational studies[23,35] on *o*-$MAPbI_3$ using deformation potential theory, taking into account differences in the temperatures considered. However, as found previously, they are much larger than experimental values, e.g. μ_e ~232 $cm^2/V{\cdot}s$ for $MASnI_3$, ~536 $cm^2/V{\cdot}s$ for $CsSnI_3$, ~66, ~25 and ~38 $cm^2/V{\cdot}s$ for $MAPbI_3$; μ_h ~105 $cm^2/V{\cdot}s$ for $MAPbI_3$.[62–64] While this may well be due to the presence of other scattering mechanisms or require methods beyond DFT (single-body theory), e.g. GW (many-body theory), the purpose of the present study is to predict trends in behavior particularly at low temperatures, as noted above.

An important feature of Figure 4 is the reduction in charge carrier mobilities for hybrid halide perovskites. This is illustrated by the black arrows which indicate how the mobilities of *o*-$MABX_3$ perovskites are reduced relative to what they would have been for hypothetical *o*-ABX_3 perovskites having the same size A-site cation. For *o*-$MAPbI_3$, for example, the reduction is nearly a factor of two (note the log scale) and this is caused by hydrogen-bonding-induced octahedral tilting. Although the MA cation increases the polycrystalline

elastic moduli (except Poisson's ratio) of hybrid halide perovskites, it also increases their average charge effective masses as shown in Figure S9. The effect on the average deformation potentials, however, is relatively small, particularly for electrons, and decreases for holes (Figure S8). According to Eq. (13), the carrier mobility μ is proportional to $m^{*-5/2}$, C and D^{-2} at a given temperature. Since the overall effect of the MA cation is to reduce the mobility, it is therefore apparent that the increase in charge effective mass is having a controlling influence. Thus, the octahedral tilting induced by the MA cation and its hydrogen-bonding interactions is directly affecting the masses of the charge carriers, as suggested in our earlier work.[10] It is clear, therefore, that to maximize the carrier mobility of a hybrid halide perovskite, the organic A-cation has to be chosen carefully so as to minimize the hydrogen-bonding interaction and the resulting rotation of the inorganic octahedra.

Conclusions

In conclusion, we have systematically calculated the elastic moduli and charge carrier mobilities of a series of halide perovskites in an effort to understand the effect of the MA organic cation on the mechanical and transport properties of hybrid perovskites. We have found that the elastic response of halide perovskites is mainly determined by the BX_3 inorganic frameworks. In addition, the unique steric and hydrogen-bonding effects introduced by the MA cation further increase the resistance of hybrid perovskites to elastic deformation. The results show that the conformation of the A-site organic cation and the strength of its hydrogen-bonding interactions with neighboring inorganic polyhedra play an important role in choosing suitable hybrid perovskites for devices with

improved mechanical stability. However, this improved mechanical stability does not result in improved carrier mobility. Using deformation potential theory within the carrier-acoustic phonon scattering regime, we have shown that the carrier mobilities of hybrid halide perovskites are in fact reduced relative to what they would have been for an inorganic perovskite having the same size A-site cation, and that this is caused primarily by octahedral tilting and a concomitant increase in charge effective mass. Nevertheless, hybrid perovskites still have mobilities comparable with inorganic perovskites and their superior mechanical stability renders them competitive in the continuing search for the optimal perovskite-based solar cell material.

Conflicts of Interest

The are no conflicts to declare.

Acknowledgments

We thank Linn Leppert and Jeffrey B. Neaton for helpful discussions. The studies were supported by the Winton Programme for the Physics of Sustainability (J-HL), the Cambridge Overseas Trust (ZD), the China Scholarship Council (ZD) and the Ras Al Khaimah Center for Advanced Materials (AKC). NCB was supported by the Royal Commission for the Exhibition of 1851, and an Imperial College Research Fellowship. The calculations were performed at the UK National Supercomputing Service, ARCHER. Access to the latter was obtained via the UKCP consortium and funded by EPSRC under Grant No. EP/P022596/1. All necessary computational data are included in the manuscript or SI.

Notes and references

1 NREL, Solar Cell Efficiency Chart, http://www.nrel.gov/ncpv/images/efficiency_chart.jpg.

2 A. Kojima, K. Teshima, Y. Shirai and T. Miyasaka, *J. Am. Chem. Soc.*, 2009, **131**, 6050–6051.

3 M. Liu, M. B. Johnston and H. J. Snaith, *Nature*, 2013, **501**, 395–398.

4 H. J. Snaith, *J. Phys. Chem. Lett*, 2013, **4**, 3623−3630.

5 H.-S. Kim, C.-R. Lee, J.-H. Im, K.-B. Lee, T. Moehl, A. Marchioro, S.-J. Moon, R. Humphry-Baker, J.-H. Yum, J. E. Moser, M. Grätzel and N.-G. Park, *Sci. Rep.*, 2012, **2**, 591.

6 T. Baikie, Y. Fang, J. M. Kadro, M. Schreyer, F. Wei, S. G. Mhaisalkar, M. Gratzel and T. J. White, *J. Mater. Chem. A*, 2013, **1**, 5628–5641.

7 M. R. Linaburg, E. T. McClure, J. D. Majher and P. M. Woodward, *Chem. Mater.*, 2017, **29**, 3507–3514.

8 A. Amat, E. Mosconi, E. Ronca, C. Quarti, P. Umari, M. K. Nazeeruddin, M. Grätzel and F. De Angelis, *Nano Lett.*, 2014, **14**, 3608–3616.

9 M. R. Filip, G. E. Eperon, H. J. Snaith and F. Giustino, *Nat. Commun.*, 2014, **5**, 5757.

10 J.-H. Lee, N. C. Bristowe, J. H. Lee, S.-H. Lee, P. D. Bristowe, A. K. Cheetham and H. M. Jang, *Chem. Mater.*, 2016, **28**, 4259–4266.

11 J.-H. Lee, N. C. Bristowe, P. D. Bristowe and A. K. Cheetham, *Chem. Commun.*, 2015, **51**, 6434–6437.

12 J. H. Lee, J.-H. Lee, E.-H. Kong and H. M. Jang, *Sci. Rep.*, 2016, **6**, 21687.

13 C. Motta, F. El-Mellouhi, S. Kais, N. Tabet, F. Alharbi and S. Sanvito,

Nat. Commun., 2015, **6**, 7026.

14 F. Brivio, K. T. Butler, A. Walsh and M. van Schilfgaarde, *Phys. Rev. B*, 2014, **89**, 155204.

15 A. Stroppa, D. Di Sante, P. Barone, M. Bokdam, G. Kresse, C. Franchini, M.-H. Whangbo and S. Picozzi, *Nat. Commun.*, 2014, **5**, 5900.

16 Y. Zhou, L. You, S. Wang, Z. Ku, H. Fan, D. Schmidt, A. Rusydi, L. Chang, L. Wang, P. Ren, L. Chen, G. Yuan, L. Chen and J. Wang, *Nat. Commun.*, 2016, **7**, 11193.

17 J. Ma and L.-W. Wang, *Nano Lett.*, 2017, **17**, 3646–3654.

18 W. Li, A. Thirumurugan, P. T. Barton, Z. Lin, S. Henke, H. H.-M. Yeung, M. T. Wharmby, E. G. Bithell, C. J. Howard and A. K. Cheetham, *J. Am. Chem. Soc.*, 2014, **136**, 7801–7804.

19 J. C. Tan and A. K. Cheetham, *Chem. Soc. Rev.*, 2011, **40**, 1059–1080.

20 J.-C. Tan, P. Jain and A. K. Cheetham, *Dalt. Trans.*, 2012, **41**, 3949–3952.

21 M. Karakus, S. A. Jensen, F. D'Angelo, D. Turchinovich, M. Bonn and E. Canovas, *J. Phys. Chem. Lett.*, 2015, **6**, 4991–4996.

22 T. M. Brenner, D. A. Egger, A. M. Rappe, L. Kronik, G. Hodes and D. Cahen, *J. Phys. Chem. Lett.*, 2015, **6**, 4754–4757.

23 Y. Wang, Y. Zhang, P. Zhang and W. Zhang, *Phys. Chem. Chem. Phys.*, 2015, **17**, 11516–11520.

24 P.-A. Mante, C. C. Stoumpos, M. G. Kanatzidis and A. Yartsev, *Nat. Commun.*, 2017, **8**, 14398.

25 S. Sun, Y. Fang, G. Kieslich, T. J. White and A. K. Cheetham, *J. Mater.*

Chem. A, 2015, **3**, 18450–18455.

26 Y. Rakita, S. R. Cohen, N. K. Kedem, G. Hodes and D. Cahen, *MRS Commun.*, 2015, **5**, 1–7.

27 J. Feng, *APL Mater.*, 2014, **2**, 081801.

28 Y.-B. Lu, X. Kong, X. Chen, D. G. Cooke and H. Guo, *Sci. Rep.*, 2017, **7**, 41860.

29 M. Sendner, P. K. Nayak, D. A. Egger, S. Beck, C. Müller, B. Epding, W. Kowalsky, L. Kronik, H. J. Snaith, A. Pucci and R. Lovrinčić, *Mater. Horiz.*, 2016, **3**, 613–620.

30 A. M. A. Leguy, A. R. Goñi, J. M. Frost, J. Skelton, F. Brivio, X. Rodríguez-Martínez, O. J. Weber, A. Pallipurath, M. I. Alonso, M. Campoy-Quiles, M. T. Weller, J. Nelson, A. Walsh and P. R. F. Barnes, *Phys. Chem. Chem. Phys.*, 2016, **18**, 27051–27066.

31 J. M. Frost, *Phys. Rev. B*, 2017, **96**, 195202.

32 A. Létoublon, S. Paofai, B. Rufflé, P. Bourges, B. Hehlen, T. Michel, C. Ecolivet, O. Durand, S. Cordier, C. Katan and J. Even, *J. Phys. Chem. Lett.*, 2016, **7**, 3776–3784.

33 A. J. Neukirch, W. Nie, J.-C. Blancon, K. Appavoo, H. Tsai, M. Y. Sfeir, C. Katan, L. Pedesseau, J. Even, J. J. Crochet, G. Gupta, A. D. Mohite and S. Tretiak, *Nano Lett.*, 2016, **16**, 3809–3816.

34 A. M. Lomonosov, X. Yan, C. Sheng, V. E. Gusev, C. Ni and Z. Shen, *Phys. status solidi - Rapid Res. Lett.*, 2016, **10**, 606–612.

35 T. Zhao, W. Shi, J. Xi, D. Wang and Z. Shuai, *Sci. Rep.*, 2016, **6**, 19968.

36 A. D. Wright, C. Verdi, R. L. Milot, G. E. Eperon, M. A. Pérez-Osorio, H.

J. Snaith, F. Giustino, M. B. Johnston and L. M. Herz, *Nat. Commun.*, 2016, **7**, 11755.

37 L. M. Herz, *ACS Energy Lett.*, 2017, **2**, 1539–1548.

38 A. Filippetti, A. Mattoni, C. Caddeo, M. I. Saba and P. Delugas, *Phys. Chem. Chem. Phys.*, 2016, **18**, 15352–15362.

39 M. A. Reyes-Martinez, A. L. Abdelhady, M. I. Saidaminov, D. Y. Chung, O. M. Bakr, M. G. Kanatzidis, W. O. Soboyejo and Y.-L. Loo, *Adv. Mater.*, 2017, **29**, 1606556.

40 Z. Deng, F. Wei, S. Sun, G. Kieslich, A. K. Cheetham and P. D. Bristowe, *J. Mater. Chem. A*, 2016, **4**, 12025–12029.

41 M. T. Weller, O. J. Weber, P. F. Henry, A. M. Di Pumpo and T. C. Hansen, *Chem. Commun.*, 2015, **51**, 4180–4183.

42 A. N. Beecher, O. E. Semonin, J. M. Skelton, J. M. Frost, M. W. Terban, H. Zhai, A. Alatas, J. S. Owen, A. Walsh and S. J. L. Billinge, *ACS Energy Lett.*, 2016, **1**, 880–887.

43 R. X. Yang, J. M. Skelton, E. L. da Silva, J. M. Frost and A. Walsh, *J. Phys. Chem. Lett.*, 2017, **8**, 4720–4726.

44 P. E. Blöchl, *Phys. Rev. B*, 1994, **50**, 17953–17979.

45 G. Kresse and D. Joubert, *Phys. Rev. B*, 1999, **59**, 1758–1775.

46 G. Kresse and J. Hafner, *Phys. Rev. B*, 1993, **47**, 558–561.

47 G. Kresse and J. Furthmüller, *Phys. Rev. B*, 1996, **54**, 11169–11186.

48 G. Kresse and J. Furthmüller, *Comput. Mater. Sci.*, 1996, **6**, 15–50.

49 G. Kresse and J. Hafner, *Phys. Rev. B*, 1994, **49**, 14251–14269.

50 J. P. Perdew, K. Burke and M. Ernzerhof, *Phys. Rev. Lett.*, 1996, **77**, 3865–3868.

51 K. Momma and F. Izumi, *J. Appl. Crystallogr.*, 2008, **41**, 653–658.

52 R. Hill, *Proc. Phys. Soc. Sect. A*, 1952, **65**, 349–354.

53 X.-Z. Li, B. Walker and A. Michaelides, *Proc. Natl. Acad. Sci.*, 2011, **108**, 6369–6373.

54 J. Bardeen and W. Shockley, *Phys. Rev.*, 1950, **80**, 72–80.

55 A. M. Glazer, *Acta Crystallogr. Sect. B Struct. Crystallogr. Cryst. Chem.*, 1972, **28**, 3384–3392.

56 A. L. Allred, *J. Inorg. Nucl. Chem.*, 1961, **17**, 215–221.

57 S. Sun, F. H. Isikgor, Z. Deng, F. Wei, G. Kieslich, P. D. Bristowe, J. Ouyang and A. K. Cheetham, *ChemSusChem*, 2017, **10**, 3740–3745.

58 R. L. Milot, G. E. Eperon, H. J. Snaith, M. B. Johnston and L. M. Herz, *Adv. Funct. Mater.*, 2015, **25**, 6218–6227.

59 T. J. Savenije, C. S. Ponseca, L. Kunneman, M. Abdellah, K. Zheng, Y. Tian, Q. Zhu, S. E. Canton, I. G. Scheblykin, T. Pullerits, A. Yartsev and V. Sundström, *J. Phys. Chem. Lett.*, 2014, **5**, 2189–2194.

60 H. Oga, A. Saeki, Y. Ogomi, S. Hayase and S. Seki, *J. Am. Chem. Soc.*, 2014, **136**, 13818–13825.

61 H. Kozuka, K. Ohbayashi and K. Koumoto, *Sci. Technol. Adv. Mater.*, 2015, **16**, 026001.

62 C. C. Stoumpos, C. D. Malliakas and M. G. Kanatzidis, *Inorg. Chem.*, 2013, **52**, 9019–9038.

63 Q. Dong, Y. Fang, Y. Shao, P. Mulligan, J. Qiu, L. Cao and J. Huang, *Science*, 2015, **347**, 967–970.

64 D. Shi, V. Adinolfi, R. Comin, M. Yuan, E. Alarousu, A. Buin, Y. Chen, S. Hoogland, A. Rothenberger, K. Katsiev, Y. Losovyj, X. Zhang, P. A.

Dowben, O. F. Mohammed, E. H. Sargent and O. M. Bakr, *Science*, 2015, **347**, 519–522.

TOC figure

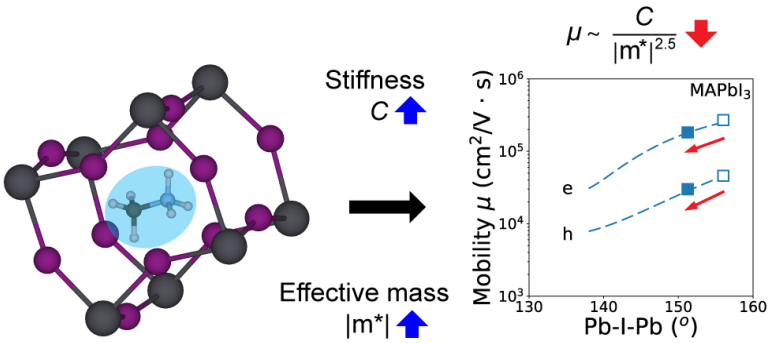
$\mu \sim \frac{C}{|m^*|^{2.5}}$
Stiffness
C
Effective mass
$|m^*|$
MAPbI$_3$
e
h
Mobility μ (cm^2/V · s)
10^6
10^5
10^4
10^3
130
140
150
160
Pb-I-Pb (°)